Interpretation of umbrella cloud growth and morphology: implications for flow regimes of short-lived and long-lived eruptions

Solène Pouget[1,†], Marcus Bursik[1], Christopher G. Johnson[2,3,*], Andrew J. Hogg[2], Jeremy C. Phillips[3], R. Stephen J. Sparks[3]

[1] Department of Geology, University of Buffalo, SUNY, Buffalo, NY, 14260, United States ([†]deceased)

[2] School of Mathematics, University of Bristol, University Walk, Bristol, BS8 1TW, United Kingdom ([*]now at School of Mathematics and Centre for Nonlinear Dynamics, University of Manchester, Oxford Road, Manchester, M13 9PL, United Kingdom)

[3] School of Earth Sciences, University of Bristol, University Walk, Bristol, BS8 1TW, United Kingdom

Corresponding author: Marcus Bursik, Department of Geology, 411 Cook Hall, University of Buffalo, Buffalo, NY, 14260, United States. email: mib@buffalo.edu. Telephone: 0017166454265, Fax: 0017166453999

Abstract

New numerical and analytical modeling shows that the growth of a volcanic umbrella cloud, expressed as the increase of radius with time, proceeds through regimes, dominated by different force balances. Four regimes are identified: Regime Ia is the long-time behavior of continuously-supplied intrusions in the buoyancy-inertial regime; Regime IIa is the long-time behavior of continuously-supplied, turbulent drag-dominated intrusions; Regime Ib is the long-time behavior of buoyancy-inertial intrusions of constant volume; and Regime IIb that of turbulent drag-dominated intrusions of constant volume. Power-law exponents for spreading time in each regime are 3/4 (Ia), 5/9 (IIa), 1/3 (Ib) and 2/9 (IIb). Both numerical modeling and observations indicate that transition periods between the regimes can be long-lasting, and during these transitions the spreading rate does not follow a simple power law. Predictions of the new model are consistent with satellite data from seven eruptions and, together with observations of umbrella cloud structure and morphological evolution, support the existence of multiple spreading regimes.

Keywords: Umbrella cloud, growth rate, intrusion, gravity current, flow regime, satellite

observations, Pinatubo, Okmok, Grímsvötn, Kelut, Redoubt, Shishaldin, Sarychev, volcanic eruption.

1. Introduction

When ash is injected into the atmosphere, its dispersal has been modeled using two different approaches. By using a Volcanic Ash Transport and Dispersal Model (VATDM) to disperse the ash in the atmosphere (e.g., Heffter and Stunder, 1993; Folch , 2012), the assumption is generally made that ash originates from a simple, arbitrary source region and will propagate as a function of the windfield and other atmospheric variables alone. By coupling an eruption column model to provide initial conditions to a VATDM (Barsotti *et al.* , 2008; Bursik *et al.*, 2012), the assumption is made that no phase of lateral ash spreading exists between eruption column rise and wind dispersal. Both of these approaches lack a key aspect of the dynamics, namely the behavior and spread as an atmospheric intrusion driven by gravity (Woods and Kienle, 1994). It has been hypothesized that the gravitational spreading of an umbrella cloud can be the driving force, depending on the intensity of the eruption, over tens to thousands of kilometers from the source (e.g., Bursik, Carey and Sparks, 1992; Sparks *et al.*, 1997; Bonadonna and Phillips , 2003; Costa, Folch and Macedonio, 2013). Lack of inclusion of gravitational spreading of ash could lead to significant mischaracterization of its transport in the atmosphere.

The goal of the present contribution is to test a new model for radial, gravity-driven intrusion of volcanic ash and gas into the atmosphere in the umbrella cloud. The model suggests the existence of distinct fluid dynamical regimes as the umbrella cloud grows with time. We test the model by careful measurement of umbrella cloud growth from satellite imagery, and comparing that growth with model output. We seek to understand whether the different fluid dynamical regimes can be observed in the data, and if so, what they imply for the dynamics of cloud growth, the quantitative values of parameters controlling that growth, and the time and distance to which gravity-driven growth can be recognized.

In the following sections, we summarize research on gravity-driven interflow within a stratified fluid, introduce the eruptions to be studied and the newly developed model of intrusion (Johnson *et al.*, 2015), which improves upon past efforts. We test the model predictions against observations for umbrella clouds produced by seven different eruptions, which allows us to assess the values of the different parameters influencing gravity flow, and the magnitude and duration of release of material into the atmosphere. Finally, we discuss implications for ash transport modeling. We also include an appendix in which a new similarity solution for the radial intrusion of a finite volume of fluid through a linearly stratified environment is constructed, in the regime where the driving gravitational forces are balance by drag.

2. Background

A buoyant plume rises vertically through an otherwise motionless environment, mixing with the surrounding fluid and eventually intrudes horizontally at its level of neutral buoyancy, where it spreads radially to form an axisymmetric cloud (see Fig. 1 and Morton *et al.* (1956)). Our study is concerned with the way in which the horizontal motion is driven by gravitational forces. This class of flow is that of a 'gravity current,' the term used for the predominantly horizontal motion of fluid of one density through surrounding fluid of another density; such motions have been widely researched for the past 60 years (see, for example, the textbooks of Simpson (1997) and Ungarish (2009), and the studies of Chen (1980) and Lemckert and Imberger (1993), which are of particular relevance for the current work).

Most previous work has used scaling techniques to identify different spreading behaviors of intrusions (Chen, 1980; Ivey and Blake, 1985; Woods and Kienle, 1994; Kotsovinos, 2000), and a small number of recent studies have used numerical modeling to better understand umbrella cloud growth (Suzuki and Koyaguchi, 2009). Several workers have compared results with data obtained from laboratory experiments (Didden and Maxworthy, 1982; Ivey and Blake, 1985; Kotsovinos, 2000), but there has been only limited comparison to full-scale natural events, notably including the study of Holasek, Self and Woods (1996), who found good agreement between a simple scaling relation and the spread of the 1991 Pinatubo (Phillipines) umbrella cloud. In general, these studies identified a power-law relationship between the radius of the intrusion and time as the intrusion grew, however, the particular value of the power-law exponent differed between studies, even for similar driving forces, and for instantaneous or continuous releases.

To summarize the fluid dynamical relationships that have been discussed by previous workers, the driving force acting on the flow is predominantly *buoyancy* (the flows are gravitationally-driven), and the resisting forces are *inertial* or *turbulent* drag. (Tables 1 and 2 show the flow regimes arising from the different combinations of these forces.) In the earliest stages of development flows may also be *momentum driven* (Chen, 1980). By *gravity driven flow*, we refer to the stage in which the flow is propagating due to gravitational effects at the level of neutral buoyancy. This stage can be divided into two phases. First, the phase in which the dominant force resisting spreading is the inertia of the displaced fluid, which we will call *inertial drag*. This regime arises in the early stage of intrusion, when the greatest difficulty in driving the relatively deep flow forward is the inertia of the air that needs to be moved out of the way. In this case, the drag force is primarily a function of the velocity of the flow front and the density of the fluid being intruded. The second regime is that in which the dominant resisting force is the drag along the interfaces (top and bottom) of the spreading current; it will be called *turbulent drag*. This regime corresponds to a flow in which the drag is a function of the velocity and the coefficient of eddy viscosity. *No drag* corresponds to the case in which the magnitude of the drag force is negligible compared to that of the driving force.

3. Data

For the purpose of this study, umbrella clouds (volcanic, radially driven intrusions into a relatively still atmosphere) from seven eruptions were studied in the visible and infrared bands in satellite images. The eruptions were chosen due to their characteristics (e.g., duration of eruption, wind speed) and availability of good quality observations (i.e., satellite imagery). On the daytime images, the diameter of the umbrella cloud was measured in eleven different directions to obtain a mean and standard deviation for the radius. The edge of the cloud was determined first by outlining from the visible band image, and then refining that outline using the brightness temperature or the infrared bands, when available (further details on this technique can be found in Pouget *et al.* (2013)). The duration of the eruption (start to cessation) was estimated from time, $t = t_0 = 0$, taken to be the start of the generation of the eruption column, using seismic and infrasound data, and ground observations when available. If the first observation consisted of satellite or ground observation of a rising plume, the time of acquisition of this image was used for the eruption start time. The difference between the time the first image was acquired after the umbrella cloud began to spread and the start of the eruption was used to estimate the uncertainty in start time, i.e., the size of the error bar in time.

The eruptions were initially divided into two groups based on eruption duration (the time during which material was injected into the atmosphere without major interruptions, not the duration of continued emissions of any type, nor the lifetime of the plume as a distinct entity in the atmosphere):

1. Group 1 – short-lived eruptions: Redoubt, 1990; Shishaldin, 1999 and Sarychev Peak,

2009.

2. Group 2 – long-lived eruptions: Pinatubo, 1991; Okmok, 2008, Grímsvötn, 2011 and Kelut, 2014.

A short-lived eruption here is defined by an injection of material into the atmosphere sustained for less than the time over which satellite observations of the plume were made, i.e., the eruption ceased before the last satellite images were acquired. A long-lived eruption lasted longer than the time of satellite acquisition. This division is important, because the intruding mass can be driven by the continued addition of new mass, as well as the gravitational forces. Long-lived eruptions cannot therefore be approximated by an instantaneous release of material. The characteristics of each eruption within its group can be found in Table 3.

3.1. Eruptions

3.1.1. Redoubt, 21 April 1990

Mount Redoubt (Alaska, USA) was active from 15 December 1989 to 21 April 1990. On that last day, at 14:12 UTC, a relatively small explosive eruption – four-minutes long, based on seismic data (Power *et al.*, 1994) – generated a pyroclastic flow that formed a large buoyant ash cloud (Woods and Kienle, 1994). The cloud was observed to rise and spread into an umbrella cloud at an altitude of 12 km ASL, by videocamera and still photography (Kienle *et al.*, 1992), with a cloud deck, top height centered around 14.6 km. The umbrella cloud tripled its radius in less than 10 minutes, and rose to its maximum altitude in about 3 minutes (Woods and Kienle, 1994). Total mass of ash in the cloud was estimated by Woods and Kienle (1994) and Pouget *et al.* (2013) as $\sim 2 \times 10^9$ kg at a temperature of 300 K. The series of photographs shows that the cloud grew with no major asymmetry, but that it had two intruding discs. The discs may be the result of a natural stratification within the cloud due to particle diffusive convection (Bursik, 1998; Carazzo and Jellinek, 2013), wherein particles concentrate at different levels based on their settling speed. We used the sketch of the outlines of the upper, more particle rich, cloud made from the original photographs and scaled by Woods and Kienle (1994).

3.1.2. Pinatubo, 15 June 1991

The eruption of Pinatubo (Luzon, Philippines) was the most intense eruption occurring during the modern satellite era. After weeks of precursory activity, a paroxysmal phase was reached on 15 June 1991 (Koyaguchi and Tokuno, 1993), which resulted in the observation of ash injected in the atmosphere for 14 hours from a plume that rose to nearly 40 km initially, but settled down to 20–25 km for an extended period, with a total of 16 h over 20 km height (Holasek, Self and Woods, 1996). Due to the powerful nature of this eruption, winds had little influence on the intruding material, therefore a large circular umbrella cloud was observed. It is uncertain when the eruption column of the paroxysmal phase started rising, since direct observations were not possible and meteorological clouds limited the observations from satellites. Based on seismic data, the first observation of a plume from the paroxysmal phase at 22:41 UTC could be the result of an eruption that produced high-amplitude tremor beginning at 22:15 UTC. Visible and infrared GMS data were available every hour, and were analyzed by Holasek, Self and Woods (1996) to show the growth of the umbrella cloud. They found that the umbrella cloud spread symmetrically for the first 4 to 5 hours before slight stretching in the East-West direction by a wind of average speed 4-5 m/s. The images used by Holasek, Self and Woods (1996) were used in this study.

3.1.3. Shishaldin, 19 April 1999

During the summer of 1998, Shishaldin (Aleutian Islands, USA) became seismically active. This activity increased until 19 April 1999, when 80 minutes of strong seismicity, starting at 19:30 UTC, was associated with a subplinian eruption (Thompson, McNutt and Tytgat, 2002). The eruption column rose to a maximum height of 16 km before dissipating within a few hours, presumably because of the high sedimentation rate of coarse particles. The spreading umbrella cloud was observed on Geostationary Operational Environmental Satellite (GOES) (Nye *et al.*, 2002).

3.1.4. Okmok, 12 July 2008

Okmok volcano (Aleutian Islands, USA) erupted on 12 July 2008 with little seismic warning. Seismic studies put the eruption start time at 19:43 UTC (Arnoult *et al.*, 2010; Johnson *et al.*, 2010). The eruption was most intense and continuous in the first ten hours (Arnoult *et al.*, 2010). A dark ash-rich plume was noticed first on GOES images at 20:00 UTC (Neal *et al.*, 2008), with an initial height of 16 km ASL (Larsen *et al.*, 2009), and which was followed an hour later by a white, vapor-rich plume. Both of these grew together into a large umbrella cloud that started being distorted by the wind at about 23:00 UTC.

3.1.5. Sarychev Peak, 14 June 2009

A MODIS image at 00:31 UTC showed a thermal anomaly and a possible weak plume at Sarychev Peak (Kurile Islands, Russia) on 11 June 2009. Later images confirmed the release of ash into the atmosphere (Rybin *et al.*, 2012). The activity, which lasted for 9 days, consisted of 23 separate explosions leading to the emission of ash plumes (Rybin *et al.*, 2009). The ash plume studied here was emitted from an eruption that began on 14 June at 18:51 UTC (Pouget *et al.*, 2013). The infrasonic data suggest eruptive activity lasting 1 h 19 min (Matoza *et al.*, 2011). The umbrella cloud grew undisturbed until 21:30 UTC, when it reached a maximum height of 16 km, before being elongated in both western and eastern directions (Levin *et al.*, 2010).

3.1.6. *Grímsvötn, 21 May 2011*

On 21 May 2011, at 19:00 UTC, Grímsvötn (Iceland), entered into a week-long explosive subglacial eruption (Petersen *et al.*, 2012). Activity was most intense during the first 10 hours, when the plume reached a momentary, maximum height of 25 km, with a sustained height of 11-19 km for 12 h. The plume eventually decreased to a 10-km height on 23 May, and finally a 5-km height on 24 May, before the end of the eruption on 28 May at 07:00 UTC (Tesche *et al.*, 2012). The umbrella cloud can first be seen at 19:15 UTC on a EUMETSAT Meteosat-9 satellite image. However, the signature of the eruption column can be observed on a satellite image taken 15 minutes earlier, and an initial explosive burst 30 minutes earlier. GOES passed over Iceland at 18:45 UTC, when no activity was observed by this lower-resolution platform, as well as 30 minutes later, when the cloud was clearly visible. During the first four hours of the eruption, four ash-rich pulses have been identified (peaks in bursts at 18:45, 19:45, 20:30 and 21:00 UTC) on imagery. Each of these pulses contributed to an umbrella cloud until 22:00 UTC, when the ash cloud became a downwind plume propagating to the south-east.

3.1.7. *Kelut, 13 February 2014*

On 13 February 2014, around 16:15 UTC, Kelut volcano erupted in Eastern Java, Indonesia. Access to satellite imagery at 10-minute intervals allowed a close study of the evolution of the eruption. During the first three hours, an umbrella cloud grew, but then quickly dispersed. The plume reached a maximum altitude of 26 km, and spread laterally at an altitude of 18 km (S. Carn, personal communication, 2014). Even though the eruption took place during the night, features interpreted to be gravity waves were observed on the upper surface of the umbrella cloud in infra-red images (E. Jannson, personal communication, 2014).

3.2. Cloud mapping

The fluid dynamical structures on satellite imagery of three of the eruptions, Okmok, Sarychev Peak and Grímsvötn, were mapped in detail, to ascertain whether any features in the eruption clouds corresponded with fluid dynamical regime. These qualitative observations in fact allowed us to recognize different dynamical behaviors during the evolution of each cloud.

On the first image from the eruption of Sarychev Peak at 18:57 UTC on 14 June, the umbrella cloud had risen above the meteorological cloud cover in a subspherical and contained (or well-defined) shape, with several irregularities identified as eddies (Fig. 2). This stage will be referred to as the *mushroom* stage, given the observed geometry of the cloud. By 19:30 UTC, the umbrella cloud had lost its subspherical shape and appeared to be wider and more flattened. This state is identified as being near the beginning of horizontal spreading. At this time, most of the umbrella cloud was still affected by eddies, particularly close to the intrusion origin. However, the distal umbrella cloud fringe was characterized by a smooth appearance (fewer eddies) and radial, finger-like edges. The smoothness is attributed to loss of turbulent energy due to loss of buoyancy, and the impact of the drag force. Gravity waves started appearing in this outer part of the umbrella, with a wavelength between 10 and 40 km around the intrusion point, and between 2 and 8 km from the intrusion point to the edge of the cloud. In this and all other imagery, wave breaking was not observed, suggesting that entrainment throughout the umbrella cloud was minimal. As time went by, the umbrella cloud became more homogeneous as eddies were less pronounced (e.g. at 19:57 UTC). The cloud became completely smooth except for gravity waves visible on the upper surface. On the last image at 20:30 UTC, only a few eddies are seen, but many concentric gravity waves are visible across the surface of the umbrella cloud, as well as in the surrounding meteorological clouds.

The first two images (18:45 and 19:00 UTC) of Grímsvötn show the rise of the eruptive column above the meteorological cloud cover (Fig. 3). At 19:15 UTC, an umbrella cloud, still attached to a visible eruptive column, started to spread horizontally. This umbrella cloud was subspherical, dark and well-contained, with an irregular surface, which is consistent with the 'mushroom' stage. Irregularities in short wave-length color suggest the presence of eddies. At 19:30, the umbrella was larger and remained subspherical, but did appear to be evolving between the mushroom and the later, "classical" umbrella stages. It was elongated in the horizontal dimensions rather than vertically. Several eddies were visible on the surface of the cloud. By 19:45 UTC, the umbrella cloud was larger and slightly less turbulent. Eddies were still visible, but the edges of the umbrella appeared to be smoother, although some radial, finger-like edges started to appear. From 20:00 to 21:00 UTC, the umbrella cloud enlarged and smoothed with time, with a possible thickening toward the leading edge. The proportion of the umbrella affected by eddies diminished, and these became confined to the area above the vent, where material continued to be intruded into the atmosphere by new bursts from the eruptive column. These new bursts were observed in images at 19:45, 20:00, 20:15 and 20:30 UTC. As the umbrella grew, gravity waves started appearing; unfortunately, a shadow obscured further observations.

The eruptive cloud from Okmok observed in the first available image at 20:00 UTC was already a large, spreading umbrella cloud, with finger-like edges; the mushroom stage was not observed (Fig. 4). The edges were quite smooth, and even though there was a small region around the intrusion point with several irregularities (i.e., eddies), most of the cloud appeared smooth, and thus, far from the mushroom stage. From 20:30 to 23:00 UTC, the umbrella cloud grew larger and wider, and gravity waves started to be visible. At 21:00, a new burst of vapor-rich material was seen intruding above the upper deck of the umbrella cloud.

4. Model

We model volcanic clouds as axisymmetric intrusions of well-mixed fluid into an otherwise quiescent, stratified atmosphere. Initially, as the rising eruption column begins to spread at the neutral buoyancy level, the flow is complex and highly turbulent with several potential mechanisms affecting the rate of spreading, including momentum-driven flow (Chen, 1980; Kotsovinos, 2000) resulting from the collapse of plume fluid that has risen above the neutral buoyancy level. This early phase we believe to correspond to our observational 'mushroom' phase or stage, as seen in the cloud mapping. However, as the cloud spreads the dynamics becomes driven by horizontal pressure gradients resulting from variations in the thickness of the intrusion. These pressure gradients are referred to by the more general term "buoyancy."

Previous studies of the buoyancy-driven spreading mechanism for intrusions are based on a box model, in which a single, characteristic cloud thickness is assumed, allowing equations of motion to be derived using force balances or scaling arguments (Lemckert and Imberger, 1993; Woods and Kienle, 1994; Costa, Folch and Macedonio, 2013). These approaches lead to the prediction that the radius of a continuously supplied plume grows as $t^{2/3}$ (Woods and Kienle, 1994), which has become widely used (Sparks *et al.*, 1997; Pouget *et al.*, 2013). However, the underlying assumption that it is possible to capture the unsteady evolution of the thickness of the cloud through a single characteristic variable is inappropriate (see Johnson *et al.* (2015)). Instead we use the analytical and numerical modeling of a buoyancy-driven intrusion developed by Johnson *et al.* (2015), which solves a complete system of 'shallow-water' equations to give the evolution of the ash cloud radius with time, as well as its thickness and radial velocity as functions of space and time. This model shows that the buoyancy-dominated state forms two distinct dynamic regimes, with different behavior close to the front from what is observed in the interior. Asymptotic solutions at late times show that the buoyancy-inertial regime in fact predict that the radius grows as $t^{3/4}$. Full numerical solutions allow us to study quantitatively the transition between different flow regimes as indicated by different asymptotic behavior, such as the onset of significant drag effects late in spread, as the buoyancy force decreases.

Full details of the modeling are reported by Johnson *et al.* (2015), but in essence the buoyancy-driven intrusion is shallow (with horizontal length scales much larger than vertical ones), implying that vertical fluid accelerations are negligible and therefore that, except near the flow front, the pressure is hydrostatic. We assume that the suspended ash is sufficiently dilute and fine that sedimentation does not cause density changes, and therefore plays no dynamic role in the radial spread of the plume. Furthermore, we assume that entrainment of air into the intrusion is negligible, once gravity-driven flow is established. We therefore consider neither sedimentation nor entrainment in this paper, although the incorporation of these is a straightforward extension to the model.

We describe the axisymmetric flow in terms of its thickness h and radial velocity u, both functions of the radial distance from source r and time t (note that h represents the thickness of the intrusion, not its altitude above the ground). These are governed by equations representing the conservation of mass and the balance of radial momentum,

$$\frac{\partial h}{\partial t} + \frac{1}{r}\frac{\partial}{\partial r}(ruh) = 0 \tag{1}$$

and

$$\frac{\partial}{\partial t}(uh) + \frac{1}{r}\frac{\partial}{\partial r}\left(ru^2h\right) + \frac{\partial}{\partial r}\left(\frac{N^2h^3}{12}\right) = -C_D u|u|, \tag{2}$$

respectively (Ungarish and Huppert, 2002; Johnson *et al.*, 2015). In (2), N denotes the buoyancy frequency of the atmosphere and the spread of the intrusion is resisted by a turbulent drag, parameterized with the coefficient C_D.

Where momentum-driven flow ends and buoyancy-driven flow begins, we must specify not only the volume flux per unit radian, $Q = ruh$, but an additional boundary condition,

r_0, the radius at which the flow is critical, i.e., the radius at which the Froude number, $Fr \equiv 2u/(Nh) = 1$. This source condition is imposed from $t = 0$ to some time t_c at which the eruption ceases; thereafter the condition applied at the source is that no further fluid enters the intrusion ($hu = 0$). At the front of the intrusion $r = r_f(t)$, vertical accelerations of fluid are non-negligible, and the forces resulting from the corresponding non-hydrostatic pressure are represented by the boundary condition $u = Fr_f Nh/2$, where Fr_f is a constant Froude number of order unity (see Ungarish, 2006, and references therein).

The governing equations (1) and (2) are hyperbolic, and may therefore develop discontinuities in the solution, here termed 'shocks'. We assume that relatively little mass or momentum is transferred between the intrusion and the ambient atmosphere at these shocks (compared with the mass and momentum fluxes of the intrusion itself), leading to the jump conditions:

$$[h(u-c)]_-^+ = 0 \qquad \text{and} \qquad \left[hu(u-c) + N^2h^3/12\right]_-^+ = 0, \tag{3}$$

where c is the radial speed of the shock and $[\ldots]_-^+$ denotes the difference between quantities either side of the shock. We use a non-oscillatory shock-capturing numerical method (Kurganov and Tadmor, 2000) to ensure that these conditions are satisfied in the numerical solutions.

By nondimensionalizing the equations and boundary conditions above with respect to the timescale N^{-1} and the lengthscale $(Q/N)^{1/3}$, the parameters Q and N are scaled out of the problem for numerical solution. Four parameters remain: the frontal Froude number, Fr_f, the dimensionless duration of the eruption, t_c, the drag coefficient, C_D, and the dimensionless source radius at which the flow is critical, r_0, which is the initial condition for the radius of the cloud. After Ungarish (2006), we set $Fr_f = 1.19$.

Our modelling of the intrusion does not include the significant vertical motions that exist within the intrusion very close to the source. For this reason we model the spreading only from the source radius onward $r \geq r_0$, and define $t = 0$ as the time when $r = r_0$.

The equations of motion (Eq 1 to 3) were solved by numerical integration. A total of 204 computational runs were performed to cover a broad range of values for the parameters and scales influencing the model output (Table 4). The values were chosen not only to assess the influence of the parameters on the result but also to reflect as much as possible the values during each of the eruptions studied for this research. It is important to remember that "duration," t_c, and "source radius," r_0, are dimensionless parameters, and their dimensional equivalents, D and R, can be calculated using the value of the timescale, i.e., $D = t_c/N$ and $R = r_0(Q/N)^{1/3}$.

5. Results

We focus first on numerical results for the theoretical growth of radius with time, and investigate the behavior with different input parameter values. Next, we compare the radial growth of the umbrella cloud according to the new numerical model with data. Finally, we investigate whether any particular power-law relationship (hence asymptotic behavior) can be seen in any given dataset.

5.1. Theoretical growth of radius with time

The radius is plotted against time in Figure 5a, for four sets of parameters: intrusions with and without drag ($C_D = 0$, $C_D = 0.01$, where 0.01 is a typical value inferred from observations; see Baines (2013)), and intrusions of short and long duration ($D = 20$ minutes and $D = 12$ hours). As plotted on logarithmic axes, a straight line of gradient α indicates a power-law relationship $r_f \sim t^\alpha$. To identify the regimes of power-law behavior, we plot the gradient of the four curves in Figure 5b. Power-law behavior is indicated on this graph by a horizontal line. We highlight with dotted lines the four regimes of power-law cloud growth, each corresponding to a long-time, asymptotic solution of the model. These regimes are: regime Ia, $r_f \sim t^{3/4}$ (upper red line), the long-time behavior of continuously-supplied, intrusions in the buoyancy-inertial regime; regime IIa, $t^{5/9}$ (upper green line), the long-time behavior of continuously-supplied, turbulent drag-dominated intrusions; regime Ib, $t^{1/3}$ (lower red line), the long-time behavior of buoyancy-inertial intrusions of constant volume, i.e., those continuing for a substantial time after the eruption has ceased, $t > D$ (Ungarish and Zemach, 2007); and regime IIb, $t^{2/9}$ (lower green line) for turbulent drag-dominated intrusions of constant volume, again at $t > D$, described in Appendix A.

Vertical lines in Figure 5 indicate the times at which the eruption stops (D), and the feeding of the intrusion ceases, i.e., volume becomes constant at that time. The rapid decrease in growth exponent shortly after these times (figure 5b) represents the slowing effect that eruption cessation has on cloud growth.

It is evident from Figure 5b that, while the behavior of the model does indeed approach these four regimes at large time, for much of the duration of the eruption, the flow is not fully in any particular asymptotic regime, and thus its effective exponent α varies with time. Of particular note is the effect of drag, which results in a slow decay of α towards its asymptotic, regime IIa value of $5/9 = 0.55\ldots$, and a lengthy period during which the cloud grows at a rate between $t^{0.6}$ and $t^{0.7}$. Observations of umbrella clouds that appear to be consistent with a $t^{2/3}$ growth rate (Woods and Kienle, 1994) may well in fact be undergoing this long transition to drag-dominated flow, with an eventual growth rate of $t^{5/9}$.

5.2. Influence of parameters

To evaluate the influence of the values of the three parameters (C_D, t_c and r_0), computations were made in which the value of one of these was changed while the values of the others were fixed (Table 4; Fig. 6). The resulting informal exploration of the parameter space, using the 204 model runs, allowed for comparison of three to ten separate outputs for each parameter. The number of outputs per parameter varied depending on ease of interpreting the resulting trends in the change in shape or position of the umbrella growth curve in (t, r)–space.

In all model runs, the cloud radius predicted by the model increases with time. At very early times, ($t \lesssim 10^2$), the spreading is strongly affected by the precise conditions at the source. Thereafter the radial spreading adopts a more universal behavior, with the fastest expansion occurring early on, before progressively slowing at later times. Two asymptotic regimes are evident from the log-log plots: a regime of relatively rapid growth while the eruption is ongoing (Regime Ia), followed by a regime after the eruption has ceased, in which the growth rate is slower (Regime Ib). These are separated by a regime transition (Fig. 5).

For comparison, we begin by looking at the effect of the buoyancy frequency, N (Fig. 6a), which is one of the primitive, dimensional variables used in the analysis. Three different values of N were tested — 0.001, 0.01 and 0.1 s^{-1}. Since N occurs in the model only through the nondimensionalization, variations of N simply result in a translation of the growth curve; a similar translation would occur with variation of V or Q. For a larger buoyancy frequency, intrusion starts sooner and the radius of the umbrella cloud with time is smaller, since the eruption column reaches the level of neutral buoyancy earlier.

Four different values of the coefficient of drag, C_D, were tested — 0.0, 0.1, 0.01 and 0.001 (Fig. 6b). The *shape* of the curve is affected by changes in C_D, and in particular a new regime is introduced (Regime IIa), in which the spreading of the cloud is dominated by turbulent drag, which becomes increasingly significant at late times. An increase in the coefficient of drag results in an earlier onset of the drag-dominated spreading regime, reducing the duration of the more rapid buoyancy-inertial spreading regime. Larger coefficients of drag diminish the growth of the umbrella cloud, both while the cloud is still growing and later, once the eruption has ceased.

The duration, t_c, of the eruption emission (Fig. 6c) directly controls the duration of the first regime of spreading (Ia). The cessation of the eruption causes the expansion rate of the cloud to decrease rapidly (towards Regime Ib), although it continues to spread. The (final) cloud volume, after the eruption has ceased, is proportional to the duration of eruption, which then acts as a scale for the radius in Regime Ib.

The last parameter was the initial, nondimensional radius of the intrusion, which was tested with three different, nondimensional values — 1, 1.5 and 2 (Fig. 6d), which are of similar magnitude to the value suggested by Baines (2013). Changes to the initial radius mainly affect the cloud radius at early times (within the first few minutes of an eruption), and rapidly become negligible as the intrusion grows to much larger radii.

At early times, the log-log plots shown here become sensitive to small offsets of the radius r or time t, which become negligible as soon as the intrusion expands to a width much greater than that of the source. The difficulty with obtaining precise predictions of the cloud behaviour at early times is compounded by the likelihood of a time-varying flux supplying the intrusion, as the plume first reaches the neutral buoyancy layer. For this reason, interpreting model results during the first few minutes of an eruption is likely to be difficult.

5.3. Fitting the new numerical model to observations

Given that a complete exploration of the parameter space for the numerical model was beyond the scope of the present contribution, output from the numerical model is directly compared with observational data for a subset of the eruptions for which reasonable fits with the numerical model were found. This constitutes a straightforward and qualitative exploration of the model, and its transitions between different flow regimes. Note there is not a unique solution in such model fitting. Here, a reasonable, illustrative set of parameters was used to estimate the conditions of the intrusion of the material in the atmosphere and its spreading by gravity (Table 5). For each of the eruptions, several outputs from the model were then explored for goodness of fit. The parameter ranges being explored in each case were chosen according to the characteristics of the eruption.

Considering the eruption of Shishaldin (Fig. 7a), fitting of the model suggests that the data are consistent with the initiation of an asymptotic flow regime. Over much of the period of observation, this umbrella cloud can be characterized by spreading as a gravity current with turbulent drag as the main resisting force in regime IIa (Table 1; Fig. 5). The growth of the umbrella cloud of Okmok is within Regime 1a (Fig. 7b), corresponding to inertial drag being the main resisting force. The model results are consistent with a drag coefficient of 0.01, and $D = 9$ hr (Table 5. The observed duration was 10 hr (Table 3). For the eruptions of both Sarychev Peak and Grímsvötn (Fig. 7c, d), a convergence from early times can be observed into Regime Ia. This suggests that the Sarychev Peak eruption was continuously fed during the period of observation. It appears there are insufficient observations to see a transition to Regime Ib. The data suggest the eruption duration for Sarychev Peak to be ~ 4740 s (Table 3), while the model is consistent with $D \sim 6000$ s. For Grímsvötn, model duration (9 hr) is likewise similar to observed (10 hr). Data from Kelut suggest a progressive transition from Regime Ia to Ib or IIa (Fig. 7e). The model eruption duration of ~ 6000 s can be compared with an observed value of ~ 10800 s. The final three observations show a decrease in radius with time within the error bars. If real, it is presumably due to dispersal of the cloud, which is not captured by the model.

For those eruptions with cloud mapping (Sarychev Peak, Okmok and Grímsvötn), the earliest time a smooth cloud top is seen in satellite imagery is indicated in Figure 7. In the case of Sarychev Peak and Okmok, asymptotic, gravity current behavior is indeed seen in the growth rate data after this time. In the case of Sarychev Peak, we can furthermore say that asymptotic behavior is not seen in imagery before this time. For Grímsvötn, however, asymptotic behavior is achieved before the appearance of the smooth cloud top. The data therefore suggest that a smooth cloud top may provide an indicator of asymptotic gravity-inertial flow.

In this set of eruptions with reasonable fits of numerical model outputs to data, non-asymptotic behavior in cloud growth, and several growth regimes, are consistent with data. For three of the eruptions, model eruption duration is quite close to observed. These results suggests that inverse modeling may yield a wealth of information about both the atmosphere and the volcanic eruption from satellite imagery. For example, volumetric flux into the umbrella cloud can be estimated ($2\pi Q$ from Table 5). The product of the pyroclast volumetric density and the integral of volumetric flux over time from 0 to D yields, of course, particle mass loading.

5.4. Asymptotic, power-law relationships observable in the data

We now explore the data further by looking for sections of growth curves for all eruptions, in which asymptotic behavior might be occurring. We then estimate best-fit asymptotes to those sections of the growth curves. This is a process fraught with uncertainty, as the numerical model suggests that asymptotic behavior can be difficult to achieve. Previous studies have assumed power-law behavior; the present study represents the first time that data are explored in sufficient detail to determine the true growth behavior. We begin by exploring the short-lived eruptions, and then look into the long-lived ones. Our goal in this section is to explore in what way the data are consistent with power-law behavior, and if so, whether there are consistent flow regimes indicated for different eruptions. Power-law fits were applied to the data after logarithmic transformation, using a least-squares regression, and the mean and standard deviation of the power-law exponent were calculated.

5.4.1. *Short-lived eruptions*

The power-law relationships for growth of intrusions into stratified fluids have been tested against the data (Fig. 8). Because it is not clear where exactly lies the temporal dividing line between an instantaneous and a continuous release, power-law relationships for both cases have been investigated for the short-lived group, and each relationship was tested to see whether it was a good match to the data.

For Redoubt, the first data point has large temporal error bars due to the ambiguity in eruption start time. Excluding this point, the best power-law fit has an exponent of 0.48 ± 0.04. For Shishaldin, all the points were considered, and the exponent of the best-fit curve is 0.22 ± 0.02, although these sparse data may be consistent with a transition in exponent towards 2/9, as suggested by the numerical results (Fig. 7a). For Sarychev Peak the exponent is 0.72 ± 0.06.

The exponents for these three short-lived eruptions are dramatically different, and are, at face value, difficult to interpret. In considering carefully that interpretation in the discussion section, we offer some potential explanations for this disparity. Here, we only conclude that no single power-law exponent is consistent with all data.

5.4.2. *Long-lived eruptions*

Since all these eruptions lasted for more than three hours, they cannot be approximated as an instantaneous release of material.

If the earliest point is ignored, data from Pinatubo have a best-fit power-law exponent of 0.72 ± 0.01 (Fig. 9). However, looking into the data more carefully, it appears that the general trend can be divided into two segments. From data point 2 to data point 8, the best power-law fit is 0.69 ± 0.02, and from data point 5 to data point 12, the best power-law fit is 0.75 ± 0.02. Note that we use overlapping data points, since the onset time of a particular flow regime is not well-defined.

The growth of the umbrella cloud of Okmok is difficult to divide into different segments. From data point 2 and lasting until the end, 0.73 ± 0.04 is the best fit.

In the case of Grímsvötn, the first data points are associated with a high value of the power-law exponent. From data point 2 to 9, the best power-law fit is 0.67 ± 0.02. If only points 2 to 5 are considered, the best power-law fit is 0.68 ± 0.05, and from data point 6 to data point 9, the best power-law fit is 0.58 ± 0.05. This decrease in power law exponent is consistent with the onset of drag (Figure 5).

Considering the eruption of Kelut, the best power-law fit for all the data is 0.54 ± 0.02. However several trends can be observed. From data point 2 to 4, the best power-law fit is 0.69 ± 0.02, then from data points 8 to 13, the power-law exponent changes to 0.40 ± 0.04, before decreasing as the result of plume dissipation.

From these observations, in addition to the idea that consistent asymptotic behavior is not necessarily the norm, it can be seen that the relationship between the radius of an umbrella cloud and time gradually evolves, as predicted by the new model. For Pinatubo and Okmok, the long-term asymptote is closest to the fraction 3/4 (Regime Ia), and for Grímsvötn and Kelut, it is closest to 5/9 (Regime IIa), after passing through 3/4.

6. Discussion

6.1. Dynamics of spreading

For short-lived eruptions, that of Redoubt is somewhat different from the others, as it originates from a distributed pyroclastic flow source rather than a point source vent. All observations for Redoubt, being taken by ground-based photography, are from much earlier in the eruption than are the satellite data acquired for the other eruptions. The best power-law fit (0.48 ± 0.04) lies between the power-laws associated with clouds of a constant volume and those associated with clouds that are continually supplied with material. This may be due to a decay of the flux being supplied to the cloud from the coignimbrite plume.

The eruptions of Sarychev Peak and Shishaldin have release durations as well as maximum plume heights and wind speeds similar to one another. However, the Shishaldin eruption was subplinian, with a powerful initial phase and decreasing mass eruption rate until the last satellite image was acquired (Caplan-Auerbach and McNutt, 2003). The entire eruption lasted for 79 min, with the first 14 min being the most intense. The single asymptotic power-law obtained for Shishaldin (0.22 ± 0.02) indicates an umbrella cloud that is no longer fed, being driven by gravity against turbulent drag (power-law of 2/9). This implies that, although at first the eruption was intense, as it weakened, negligible additional material was being added and intruding in the atmosphere. This may explain the low value of the modeled duration (Table 5). In the case of Sarychev Peak, the power-law relationship is consistent with a continuously-fed umbrella cloud spreading as a gravity current dominated by inertial drag (power-law of 3/4). It appears that on the time-scale of the available satellite imagery, this particular eruption continued to be fed substantially from the vent, and that the difference with Shishaldin is therefore that the intensity of the release was more or less constant over the time, suggesting that it is perhaps better classified with the continuous eruptions.

Among the eruptions that were more clearly continuous, the results for Pinatubo are ambiguous, being consistent with either the previously accepted or the present model. The best-fit (single) power-law exponent of 0.72 ± 0.01 is between that for the previously accepted model ($2/3 \sim 0.667\ldots$) and the present model ($3/4 = 0.75$) for the buoyancy-inertial regime (Ia).

For Okmok and Grímsvötn, the best fit is consistent with a slope changing to $r_f \sim t^{3/4}$, then to $r_f \sim t^{5/9}$ with time (regime Ia to IIa). This corresponds to a transition between a gravity current spreading in the 'buoyancy-inertial' regime with inertial drag as the main resisting force, to one in which turbulent drag resists buoyancy forces. For both eruptions, it is found that $r_f \sim t^{2/3}$ is a good approximation for the entire trend, as $2/3 \approx 0.67$ lies between $3/4 = 0.75$ and $5/9 \approx 0.56$. We suggest that this approximation is not the result of the presence of a separate asymptotic regime, as suggested by Woods and Kienle (1994), but results from a transition between the inertial $t^{3/4}$ and turbulent drag-dominated $t^{5/9}$ regimes. This means that although observational data may best be described by the transition in behavior as predicted by our numerical model, the agreement of observations with the $t^{2/3}$ trend may be expected, given typical measurement errors (e.g. Holasek, Self and Woods, 1996). Using a $t^{2/3}$ regime to fit the data would, however, result in degraded estimation of values of the eruption parameters.

For the 2014 eruption of Kelut, with a greater number of observations, best fits indicate the establishment of a $r_f \sim t^{3/4}$ regime (Ia), changing to $r_f \sim t^{5/9}$ (regime IIa). The higher-quality data for Kelut are inconsistent with a relationship of $r_f \sim t^{2/3}$. Note that the last observations of the Kelut eruption indicate a reduction in radius, corresponding to rapid dispersion of the umbrella cloud.

Comparing the evolution of the radius with time for different eruptions, we conclude that there is not just one relationship between radius and time and that the relationship changes gradually. Thus, the use of the new model, capable of reproducing the transitions in spreading rate, is potentially important, as the model predicts times of transition, as well as the progression from one type of power-law behavior to another, based on different parameter values. Model curve-fitting should thus provide an estimate for the values of the parameters.

6.2. Regime transitions and cloud maps

For a typical isolated volcanic thermal or starting plume, a rise height of 12 km is reached after c. 400 seconds from the beginning of the eruption (Sparks *et al.*, 1997). Therefore, in the case of Sarychev Peak, Okmok and Grímsvötn, it is expected that the plume would take more than five minutes to rise, before beginning to intrude laterally into the atmosphere. The clouds from both Sarychev Peak and Grímsvötn were observed on the first satellite image one to five minutes from the beginning of the eruption, at 360 and 90 seconds, respectively (Fig. 2, 3). As a result, these first observations are not of an umbrella cloud spreading as a gravity current, but of an earlier, potentially momentum-dominated spread. This growth phase corresponds to a 'mushroom' structure with (turbulence related) irregularities (Figs. 2, 3, 4).

Following the 'mushroom' phase, the buoyancy-driven intrusion phase develops. On satellite imagery, the transition to gravity driven flow is not extremely well-defined, as the subspherical cloud turns into a spreading umbrella. This might be the result of the acquisition time between images. For Okmok and Sarychev Peak, a satellite image was available every 30 min during the eruption, and for Gímsvötn, it was every 15 min. Good agreement with our model after the first observation suggests that the spreading becomes predominantly buoyancy-driven in less than 15 min for the examples of Sarychev Peak and Grímsvötn (Fig. 7).

The buoyancy-driven growth phase corresponds to the time when the umbrella cloud is observed to smooth and widen. This phase of spreading can be divided in two periods, given the structures observed in the umbrella. In the first period, the umbrella has several irregularities due to the presence of eddies, and the irregularities of the edges are defined as being finger-like. In the second period, the umbrella cloud develops a smooth appearance, with non-fingering edges and gravity waves on the upper surface. The first period is observed for the eruptions of Okmok, from 20:00 to about 20:30 UTC, for Sarychev Peak from 19:30 to 19:57 UTC and for Grímsvötn from 19:30 to about 19:45 UTC. This timing corresponds to the gradual transition between the different regimes, in which $r_f \sim t^{3/4}$ (Regime Ia) is reached for the eruptions of Okmok from about 20:30 to 23:00 UTC, for Sarychev Peak from 19:57 to 20:57 UTC and for Grímsvötn from about 19:45 to 20:45 UTC.

After this, another transition occurs as turbulent drag begins to dominate. The effect of turbulent drag is characterized by a relationship of either $r_f \sim t^{2/9}$ (Regime IIb) for instantaneous eruptions, or $r_f \sim t^{5/9}$ (Regime IIa) for long-lived eruptions.

Transition to Regime II is observed on the satellite images by an enlarged and smoothed umbrella cloud surface affected by numerous concentric gravity waves (e.g. Fig. 3). These gravity waves can also affect the surrounding meteorological clouds (Fig. 2). In this regime, eddies are not detected, as they are disappearing from the cloud. Although the Regime II power-law exponents from the numerical model runs are consistent with the data for several eruptions, only those data for Shishaldin captured transition to this behavior, given the parameter values explored and the duration of the transition from one regime to another.

6.3. Implications for ash clouds and forecasting

The new model captures the evolution of the radius with time when an ash cloud intrudes in the atmosphere, and the transition from one spreading regime to another. This has a rather important implication for ash cloud forecasting. The way ash clouds are simulated at the operational level in near-real time is either by dispersing the ash once it is introduced at height, using one of several VATDMs, such as HYSPLIT or NAME (Folch , 2012), or by simulating first the injection of the ash into the atmosphere using a column model and then using a VATDM, such as in VOLCALPUFF or puffin (Barsotti *et al.* , 2008; Bursik *et al.*, 2012). Neither of these two standard procedures includes the spread of the ash in a gravity current. This could be an issue, since it has been shown that the spreading as a gravity current can occur hundreds to thousands of kilometers from the source, depending on the mass eruption rate and the column height (Bursik, Carey and Sparks, 1992; Pouget *et al.*, 2013; Costa, Folch and Macedonio, 2013). The results of the present contribution suggest that the refinements introduced herein would provide an improved basis for the physics of the gravity current. Adding an implementation of the new model into a dispersion model would enable the behavior of ash in the atmosphere to be better captured, and a better estimation of parameters needed for the atmospheric dispersal calculation, such as mass loading, spatial distribution of ash, effective buoyancy frequency, and atmospheric level of spreading.

7. Conclusions

We tested a new numerical model of a spreading volcanic umbrella cloud. The model is based on careful consideration of the spreading cloud front, and predicts the occurrence of different spreading regimes. Data for seven different eruptions are consistent with the new model. Each of the spreading regimes can be expressed with a different power-law exponent in asymptotic analysis, although numerical modeling suggests that these asymptotic flows can take considerable time to develop. We have shown that a simpler model, based on a single velocity scaling relationship, does not capture this behavior, and cannot fit all available data, being consistent with only a single spreading regime and a single power-law exponent. Using least-squares fitting, we have shown that the new numerical model fits all available satellite data. Perhaps more importantly, we have shown strong support for the model and the existence of the flow regimes by creating histories for the growth of umbrella clouds from numerous eruptions consistent with known timing information, measured growth rates, and cloud mapping. Furthermore, the detailed growth curve for a spreading umbrella cloud is sensitive to a number of parameters, including mass eruption rate and eruption duration. Limited numerical curve fitting suggests that both atmospheric and volcanic parameters can be estimated from cloud growth curves.

Furture research should include effects of sedimentation and entrainment of air. Nye *et al.* (2002) show, e.g., that the cloud of Shishaldin dissipated rapidly because of sedimentation of coarse pyroclasts. Intuitively, entrainment should be important in some situations where the breaking jump at the back of the intrusion head brings in substantial mass relative to the starting mass of the intrusion.

Acknowledgments. This research was supported by NSF-IDR CMMI grant number 1131074 to E. B. Pitman, and by AFOSR grant number FA9550-11-1-0336 to A.K. Patra. All results and opinions expressed in the foregoing are those of the authors and do not reflect opinions of NSF or AFOSR. CGJ, AJH, JCP and RSJS acknowledge support from NERC (UK) through the Vanaheim project "Characterisation of the near-field Eyjafjallajokull volcanic plume and its long-range influence" (NE/I01554X/1). AJH and JCP were additionally funded by the European Union Seventh Framework Programme (FP7, 2007-2013) under grant agreement number 208377, FutureVolc, and AJH and CGJ by EPSRC (UK) through grant EP/G066353/1. The authors would like to thank Peter Webley, Jon Dehn, Emile Jansons and Andrew Tupper for giving us access to satellite imagery. We would like to thank Greg Valentine and the reviewers (Tak Koyaguchi and an anonymous reviewer) for their useful comments, which greatly improved the manuscript. The paper is dedicated to the memory of Solène Pouget, an exemplary young scientist and human being.

Arnoult, K.M., Olson, J.V., Szuberla, C.A.L., McNutt, S.R., Garces, M.A., Fee, D. and Hedlin, M.A.H., 2010. Infrasound observations of the 2008 explosive eruptions of Okmok and Kasatochi Volcanoes, Alaska. Journal of Geophysical Research, 115, D00L15

Baines, P.G., 2013. The dynamics of intrusions into a density-stratified crossflow. Physics of Fluids, 25, 076601

Barsotti, S., A. Neri, and J. S. Scire (2008), The VOL-CALPUFF model for atmospheric ash dispersal: 1. Approach and physical formulation, J. Geophys. Res., 113, B03208, doi:10.1029/2006JB004623.

Bonadonna, C., Genco, R., Gouhier, M., Pistolesi, M., Cioni, R., Alfano, F., Hoskuldsson, A. and Ripepe, M., 2011. Tephra sedimentation during the 2010 Eyjafjallajkull eruption (Iceland) from deposit, radar, and satellite observations. Journal of Geophysical Research, 116, B12202

Bonadonna C, Phillips JC (2003) Sedimentation from strong volcanic plumes. J Geophys Res 108(B72340) doi:10.1029/2002JB002034

Bursik, M., 1998. Tephra dispersal *in* The Physics of Explosive Volcanic Eruptions (J.S. Gilbert and R.S.J. Sparks, eds.). Geol. Soc. London Spec. Pub. 145, 115-144

Bursik, M.I., Carey, S.N. and Sparks, R.S.J., 1992. A gravity current model for the May 18, 1980 Mount-St-Helens plume, Geophysical Research Letters, 19(16), 1663-1666

Bursik, M.I., Jones, M.D., Carn, S., Dean, K., Patra, A.K., Pavolonis, M., Pitman, E.B., Singh, T., Singla, P., Webley, P., Bjornsson, H. and Ripepe, M., 2012. Estimation and propagation of volcanic source parameter uncertainty in an ash transport and dispersal model Application to the Eyjafjallajokull plume of 14-16 April 2010. Bulletin of Volcanology, 74, 2321-2338, doi:10.1007/s00445-012-0665-2

Caplan-Auerbach, J. and McNutt, S.R., 2003. New insights into the 1999 eruption of Shishaldin volcano, Alaska, based on acoustic data. Bulletin of Volcanology, 65, 405-417

Carazzo, G. and Jellinek, A.M., 2013. Particle sedimentation and diffusive convection in volcanic ash-clouds. Journal of Geophysical Research: Solid Earth, 118, 1420-1437. DOI:10.1002/jgrb.50155

Chen, J.C., 1980. Studies on gravitational spreading currents. PhD thesis, California Institute of Technology.

Costa, A., Folch, A. and Macedonio, G., 2013. Density-driven transport in the umbrella region of volcanic clouds: implications for tephra dispersion models. Geophysical Research Letters, 40, 1-5

Didden, N. and Maxworthy, T., 1982. The viscous spreading of plane and axisymmetric gravity currents. Journal of Fluid Mechanics, 121, 27-42

Folch, A. (2012). A review of tephra transport and dispersal models: evolution, current status, and future perspectives. Journal of Volcanology and Geothermal Research, 235, 96-115.

Garvine, R.W., 1984. Radial spreading of buoyant, surface plumes in coastal waters. Journal of Geophysical Research, 89, 1989-1996

Heffter, J.L. and Stunder, B.J., (1993). Volcanic ash forecast transport and dispersion (VAFTAD) model. Weather and Forecasting, 8(4), 533-541.

Holasek, R.E., Self, S. and Woods, A.W., 1996. Satellite observations and interpretation of the 1991 Mount Pinatubo eruption plumes. Journal of Geophysical Research, 101, B12, 27,635-27,655

Ivey, G.N. and Blake, S., 1985. Axisymmetrical withdrawal and inflow in a density-stratified container. Journal of Fluid Mechanics, 161, 115–137.

Johnson, C.G., Hogg, A.J., Huppert, H.E., Sparks, R.S.J., Phillips, J.C., Slim, A.C. and Woodhouse, M.J., 2015. Modelling intrusions through quiescent and moving ambients. Journal of Fluid Mechanics, 771, 370–406, doi:10.1017/jfm.2015.180

Johnson, J.H., Prejean, S.G., Savage, M.K. and Townend, J., 2010. Anisotropy, repeating earthquakes, and seismicity associated with the 2008 eruption of Okmok Volcano, Alaska. Journal of Geophysical Research, 115, B00B04

Kienle, J., Woods, A.W., Estes, S.A. and Ahlnaes, K., 1992. Satellite and slow-scan television observations of the rise and dispersion of ash-rich eruption clouds from Redoubt volcano, Alaska. Proceedings of the International Conference on the Role of Polar Regions in Global Change, Fairbanks, Alaska on 11-15 June 1990. In Technical Report AD-A253-028, 748-750.

Kotsovinos, N.E., 2000. Axisymmetric submerged intrusion in stratified fluid. Journal of hydraulic engineering, 126, 446-456

Koyaguchi, T. and Tokuno, M., 1993. Origin of the giant eruption cloud of Pinatubo, June 15, 1991. Journal of Volcanology and Geothermal Research, 55(1-2), 85-96

Kurganov, A. and Tadmor, E., 2000. New high-resolution central schemes for nonlinear conservation laws and convectiondiffusion equations. Journal of Computational Physics, 160(1), 241-282.

Larsen, J., Neal, C., Webley, P., Freymueller, J., Haney, M., McNutt, S.R., Schneider, D., Prejean, S., Schaefer, J. and Wessels, R., 2009. Eruption of Alaska volcano breaks historic pattern. Eos, Transactions, American Geophysical Union, 90, 20, 173-174

Lemckert, C. J. and Imberger, J., 1993. Axisymmetric intrusive gravity currents in linearly stratified fluids. Journal of Hydraulic Engineering, 119, 662-679.

Levin, B.W., Rybin, A.V.; Vasilenko, N.F., Prytkov, A.S., Chibisova, M.V., Kogan, M.G., Steblov, G.M. and Frolov, D.I., 2010. Monitoring of the eruption of the Sarychev Peak Volcano in Matua Island in 2009 (central Kurile Islands). Doklady Earth Sciences, 435(1), 1507-1510

Matoza, R.S., Le Pichon, A., Vergoz, J., Herry, P., Lalande, J-M., Lee, H-I., Che, I-Y. and Rybin, A., 2011. Infrasonic observations of the June 2009 Sarychev Peak eruption, Kuril Islands: implications for infrasonic monitoring of remote explosive volcanism. Journal of Volcanology and Geothermal Research, 200, 35-48

Maxworthy, T., Leilich, J.; Simpson, J.E. and Meiburg, E.H., 2002. The propagation of a gravity current into a linearly stratified fluid. Journal of Fluid Mechanics, 453, 371-94

Morton, B. R., Taylor, G. and Turner, J. S., 1956. Turbulent gravitational convection from maintained and instantaneous sources. Proceedings of the Royal Society of London. Series A. Mathematical and Physical Sciences, 234(1196), 1-23.

Neal, C.A., McGimsey, R.G., Dixon, J.P., Cameron, C.E., Nuzhdaev, A.A., Chibisova, M., 2011. 2008 volcanic activity in Alaska, Kamchatka, and the Kurile Islands; summary of events and response of the Alaska Volcano Observatory. USGS Scientific Investigations Report, 94.

Nye, C.J., Keith, T.E.C., Eichelberger, J.C., Miller, T.P., McNutt, S.R., Moran, S., Schneider, D.J., Dehn, J. and Schaefer, J.R., 2002. The 1999 eruption of Shishaldin Volcano, Alaska: monitoring a distant eruption. Bulletin of Volcanology, 64, 507-519.

Petersen, G.N., 2010. A short meteorological overview of the Eyjafjallajokull eruption 14 April – 23 May 2010, Weather, 65, 203-207, doi:10.1002/wea.634

Petersen, G.N., Bjornsson, H., Arason, P. and von Löwis, S., 2012. Two weather radar time series of the altitude of the volcanic plume during the May 2011 eruption of Grímsvötn, Iceland. Earth System Science Data, 4, 121-127.

Pouget, S., Bursik, M., Webley, P., Dehn, J. and Pavolonis, M., 2013. Estimation of eruption source parameters from umbrella cloud or downwind plume growth rate. Journal of Volcanology and Geothermal Research, 258, 100-112.

Power, J.A., Lahr, J.C., Page, R.A., Chouet, R.A., Stephens, C.D., Harlow, D.H., Murray, T.L. and Davies, J.N., 1994. Seismic evolution of the 1989-1990 eruption sequence of Redoubt volcano, Alaska. Journal of Volcanology and Geothermal Research, 62, 69-94

Rybin, A.V., Chibisova, M.V., Webley, P., Steensen, T., Izbekov, P., Neal, C. and Realmuto, V., 2011. Satellite and ground observations of the June 2009 eruption of Sarychev Peak Volcano, Matua Island, central Kuriles. Bulletin of Volcanology, 73, 9, 1377-1392

Rybin, A.V., Razjigaeva, N., Degterev, A., Ganzey, K. and Chibisova, M.V., 2012. The Eruptions of Sarychev Peak Volcano, Kurile Arc: Particularities of Activity and Influence on the Environment, New Achievements in Geoscience. Dr. Hwee-San Lim (Ed.), ISBN: 978-953-51-0263-2

Simpson, J.E. 1997 Gravity currents in the environment and the laboratory. Cambridge University Press, pp. 244

Sparks, R.S.J., Moore, J.G. and Rice, C.J., 1986. The initial giant umbrella cloud of the May 18th, 1980, explosive eruption of Mount St. Helens. Journal of Volcanology and Geothermal Research, 28(3-4), 257-274

Sparks, R.S.J., Bursik, M.I., Carey, S.N., Gilbert, J.S., Glaze, L.S., Sigurdsson, H. and Woods, A.W., 1997. Volcanic Plumes. Wiley, New York.

Suzuki, Y.J. and Koyaguchi, T., 2009. A three-dimensional numerical simulation of spreading umbrella clouds. Journal of Geophysical Research: Solid Eart, 114(B3).

Tesche, M., Glantz, P., Johansson, C., Norman, M., Hiebsch, A., Ansmann, A., Althausen, D., Engelmann, R. and Seifert, P., 2012. Volcanic ash over Scandinavia originating from the Grímsvötn eruptions in May 2011. Journal of Geophysical Research, 117, D09201, doi: 10.1029/2011JD017090.

Thompson, G., McNutt, S.R. and Tytgat G., 2002. Three distinct regimes of volcanic tremor associated with the eruption of Shishaldin Volcano, Alaska 1999. Bulletin of Volcanology, 64, 535-547.

Ungarish, M.,2006. On gravity currents in a linearly stratified ambient: a generalization of Benjamins steady-state propagation results. Journal of Fluid Mechanics, 548, 49-68.

Ungarish, M.,2009. An introduction to gravity currents and intrusions, CRC Press, pp. 489.

Ungarish, M. and Huppert, H. E., 2002. On gravity currents propagating at the base of a stratified ambient. Journal of Fluid Mechanics, 458, 283-301.

Ungarish, M. and Zemach, T., 2007. On axisymmetric intrusive gravity currents in a stratified ambient - shallow-water theory and numerical results. European Journal of Mechanics B/Fluids, 26, 220-235.

Waythomas, C.F., Scott, W.E., Prejean, S.G., Schneider, D.J., Izbekov, P. and Nye, C.J., 2010. The 7-8 August 2008 eruption of Kasatochi Volcano, central Aleutian Islands, Alaska. Journal of Geophysical Research, 115, B00B06

Woods, A.W. and Kienle, J., 1994. The dynamics and thermodynamics of volcanic clouds: Theory and observations from the april 15 and april 21, 1990 eruptions of redoubt volcano, Alaska. Journal of Volcanology and Geothermal Research, 62(1-4), 273-299

Tables and Table Captions

Table 2: Relationships between r_f, and t for continuous releases.

Regime	Resisting force	$r_f(t)$	Method	Reference
	Inertial drag (constant flow thickness)	$r_f \sim t^{1/2}$	Scaling	Ivey and Blake 1985
	Inertial drag	$r_f \sim t^{2/3}$	Scaling	Chen 1980, Lemckert and Imberger 1993, Woods and Kienle 1994
Ia	Inertial drag	$r_f \sim t^{3/4}$	Analytical	Johnson *et al* 2015, **this study**
IIa	Turbulent drag	$r_f \sim t^{5/9}$	Analytical	Johnson *et al* 2015, **this study**

Table 1: Relationships between r_f, and t for instantaneous releases.

Regime	Resisting force	$r_f(t)$	Method	Reference
Ib	Inertial drag	$r_f \sim t^{1/3}$	Numerical, observational	**This study**
			Numerical, analytical	Ungarish and Zemach 2007
			Scaling	Sparks *et al* 1997
IIb	Turbulent drag	$r_f \sim t^{2/9}$	Analytical	**This study**

Table 3: Eruption characteristics of duration, plume height (ASL) and wind speed at plume height (ms^{-1}).

Group	Eruption	Duration	Maximum plume height (km)	Neutral buoyancy level (km)	Wind speeds (ms^{-1})
Group 1	Redoubt, 1990	4 min		12	8
short-lived	Shishaldin, 1999	1h20 min		14	6
	Sarychev Peak, 2009	1h19 min	16		5
Group 2	Pinatubo, 1991	14h	37-40		4-5
long-lived	Okmok, 2008	10h	16		5-8
	Grímsvötn, 2011	10h	25 (sustained 11-19)		8-9
	Kelut, 2014	3h	26	18	8-9

Table 4: Dimensionless parameters and conditions of the different numerical runs.

Parameter	Values
Coefficient of drag, C_D	0; 0.001; 0.01; 0.1
Duration, t_c	2; 4; 6; 8; 10; 12; 14; 16; 18; 24; 30; 36; 72; 288; 324
Source radius, r_0	1; 1.5; 2

Table 5: Parameter values used to reproduce with the model the observed growth of radius with time. Bold indicates best fit model.

Eruption	Curve color	N (s^{-1})	C_D	t_c	Q ($m^3 s^{-1} rad^{-1}$)	r_0
Shishaldin, 1999	Green	0.05	0.1	2	2×10^8	2
	Blue	0.05	0.1	2	1×10^8	2
	Red	0.05	0.1	2	9×10^7	2
Okmok, 2008	Orange	0.01	0.01	324	2×10^8	1.5
	Green	0.01	0.01	324	1.5×10^8	1.5
	Blue	0.01	0.01	324	1×10^8	1.5
Sarychev Peak, 2009	Red	0.002	0.1	12	4×10^8	2
	Blue	0.002	0.1	12	3×10^8	2
Grímsvötn, 2011	Blue	0.01	0.1	324	1×10^9	1.5
	Red	0.01	0.1	324	8×10^8	1.5
	Black	0.01	0.1	324	6×10^8	1.5
	Green	0.01	0.1	324	5×10^8	1.5
Kelut, 2014	Red	0.1	0.1	324	2×10^9	1.5
	Blue	0.1	0.1	324	1×10^9	1.5
	Green	0.1	0.1	324	9×10^8	1.5

Figures and Figure Captions

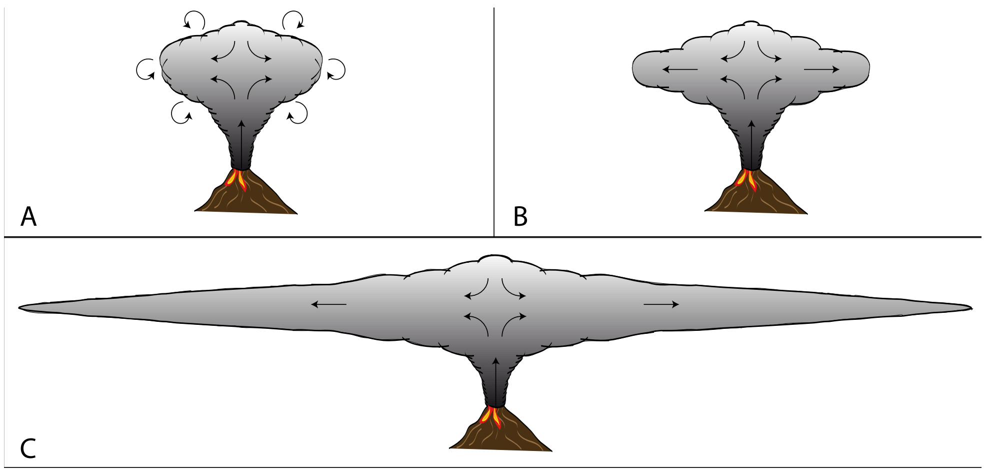

Figure 1: Sketch of intruding volcanic umbrella cloud spreading as a gravity current in a stratified environment with no or negligible winds. (a) The intruding cloud with momentum as driver is represented by large and numerous eddies, as well as entrainment. After this, umbrella cloud spreading is driven by buoyancy. (b) First phase of buoyant spreading is resisted by inertial drag, with fewer eddies. (c) The second phase is resisted by drag, in which umbrella spreads as a thin, laminar layer.

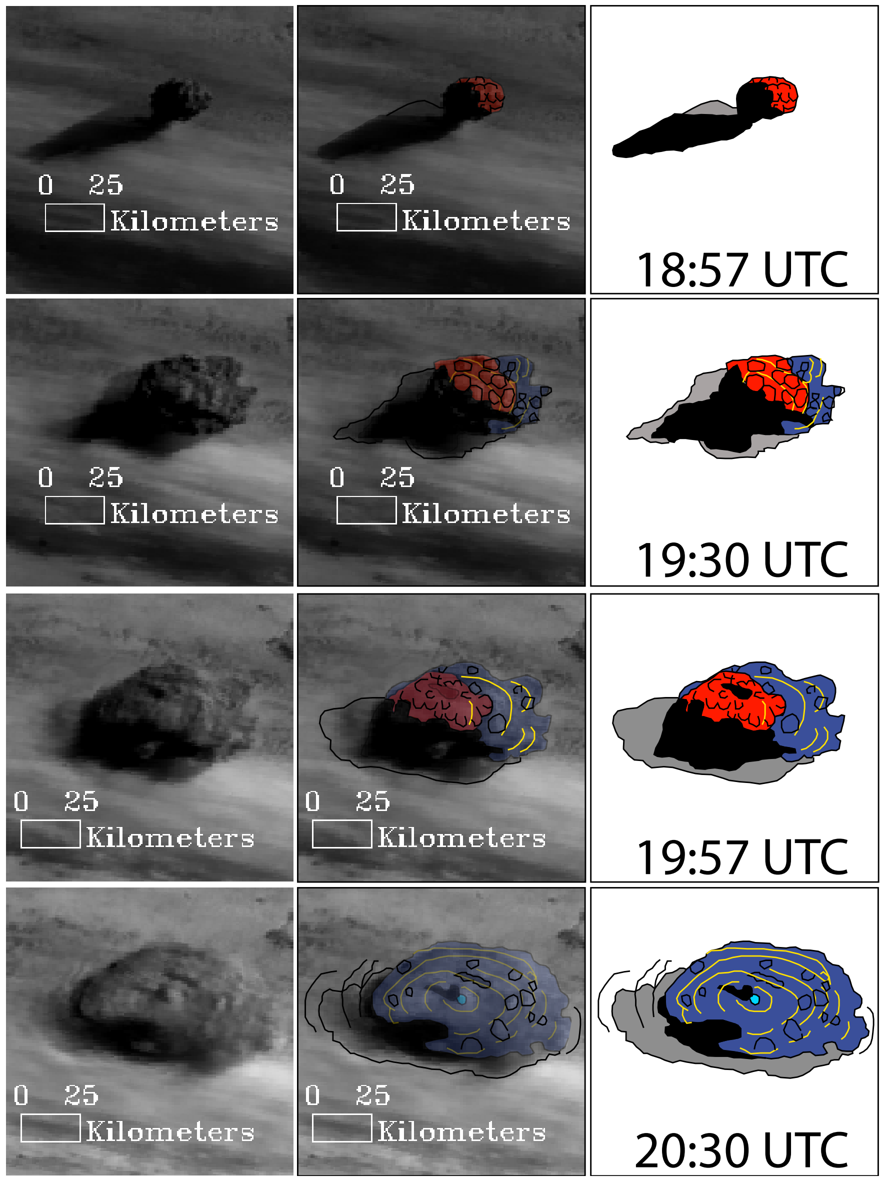

Figure 2: Evolution of the Sarychev Peak eruptive cloud with time in visible band, visible band with mapping overlayed, and mapping (from left to right). Eddies visible in the umbrella are outlined in black, gravity waves are mapped by a bright yellow line placed at the wave trough. New bursts into the cloud are represented with light blue. The part of the umbrella with eddies is colored in red, while the part with few to no eddies is coloured in dark blue. Any dense shadow is coloured in black, and light shadow is grey.

Figure 3: Evolution of the Grímsvötn eruptive cloud with time in visible band from low viewing angle (causing cloud to appear elongated), visible band with mapping overlayed, and mapping (from left to right). Eddies visible in the umbrella are outlined in black, gravity waves are mapped by a bright yellow line placed at the wave trough. New bursts into the cloud are represented with light blue. The part of the umbrella with eddies is colored in red, while the part with few to no eddies is coloured in dark blue. Any dense shadow is coloured in black, and light shadow is grey.

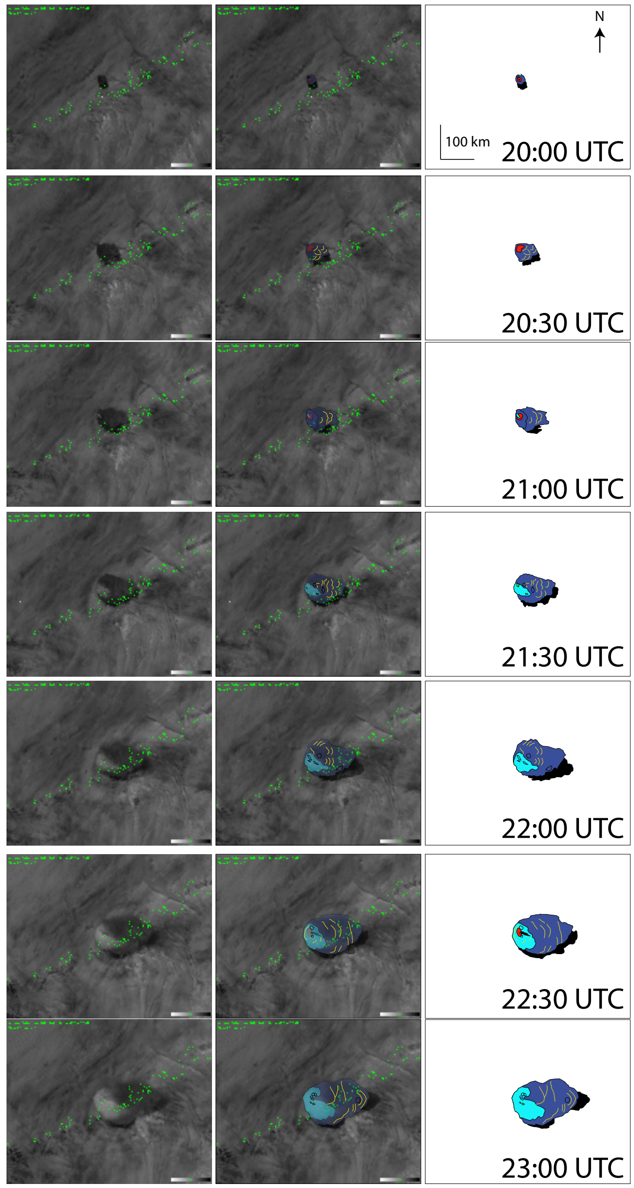

Figure 4: Evolution of the Okmok eruptive cloud with time in visible band, visible band with mapping overlayed, and mapping (from left to right). Eddies visible in the umbrella are outlined in black, gravity waves are mapped by a bright yellow line placed at the wave trough. New bursts into the cloud are represented with light blue. The part of the umbrella with eddies is colored in red, while the part with few to no eddies is coloured in dark blue. Any dense shadow is coloured in black, and light shadow is grey.

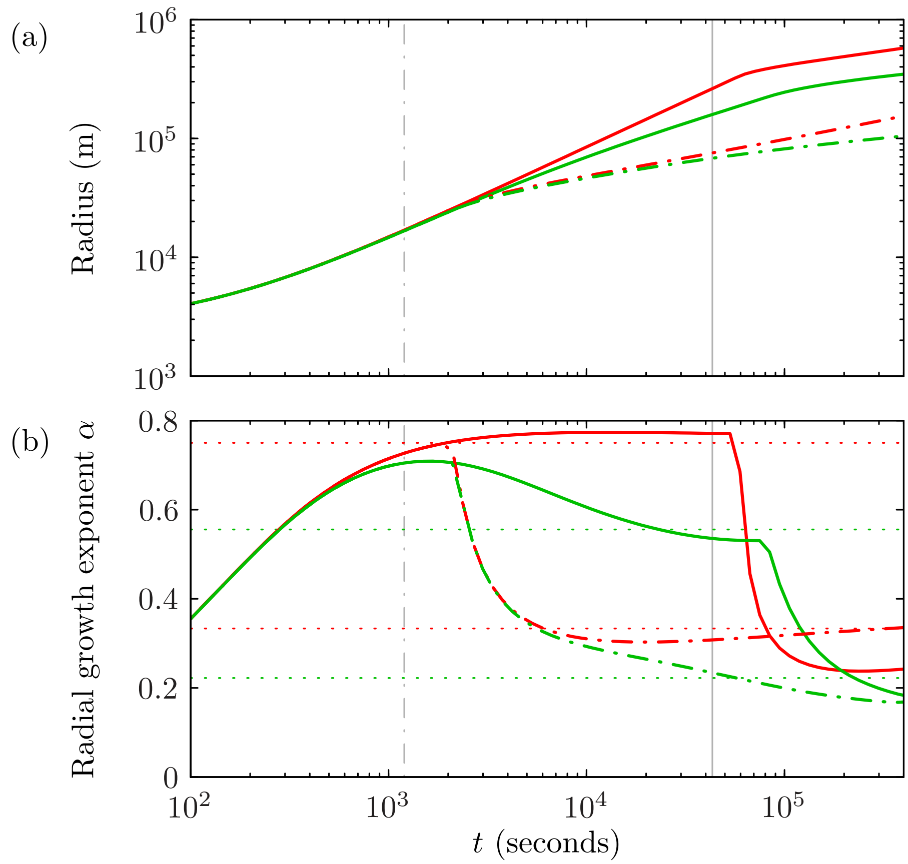

Figure 5: (a) Plots of current radius r_f as a function of time, determined from numerical solution of Eqns (1) and (2). (b) Plots of $\mathrm{d}\log(r_f)/\mathrm{d}\log(t)$, gradient of r_f against t on logarithmic axes. Regimes where curves in (b) take a constant value indicate straight-line regimes of curves in (a), hence regimes where radial growth with time is well matched by a power law, $r_f \sim t^{\alpha}$. Results for four sets of parameters are plotted, each with $N = 0.01$ s^{-1} and $2\pi Q = 10^9\,\mathrm{m}^3\,\mathrm{s}^{-1}$. Red curves indicate solutions with no drag ($C_D = 0$), and green curves indicate those with $C_D = 0.01$. For solid curves, the intrusion is supplied between $t = 0$ and $t_c = 432$ nondimensional units, corresponding to an eruption duration, $D = 12$ hours; for dash-dotted curves, source is turned off at $t_c = 12$ nondimensional units, corresponding to an eruption duration, $D = 20$ minutes. These times are represented by vertical grey solid and dash-dotted lines, respectively. Horizontal dotted lines in (b) indicate the long-time asymptotes for r_f of $t^{3/4}$ (upper red line), $t^{5/9}$ (upper green line), $t^{1/3}$ (lower red line) and $t^{2/9}$ (lower green line). The numerical results asymptote to these curves at times much greater than those shown.

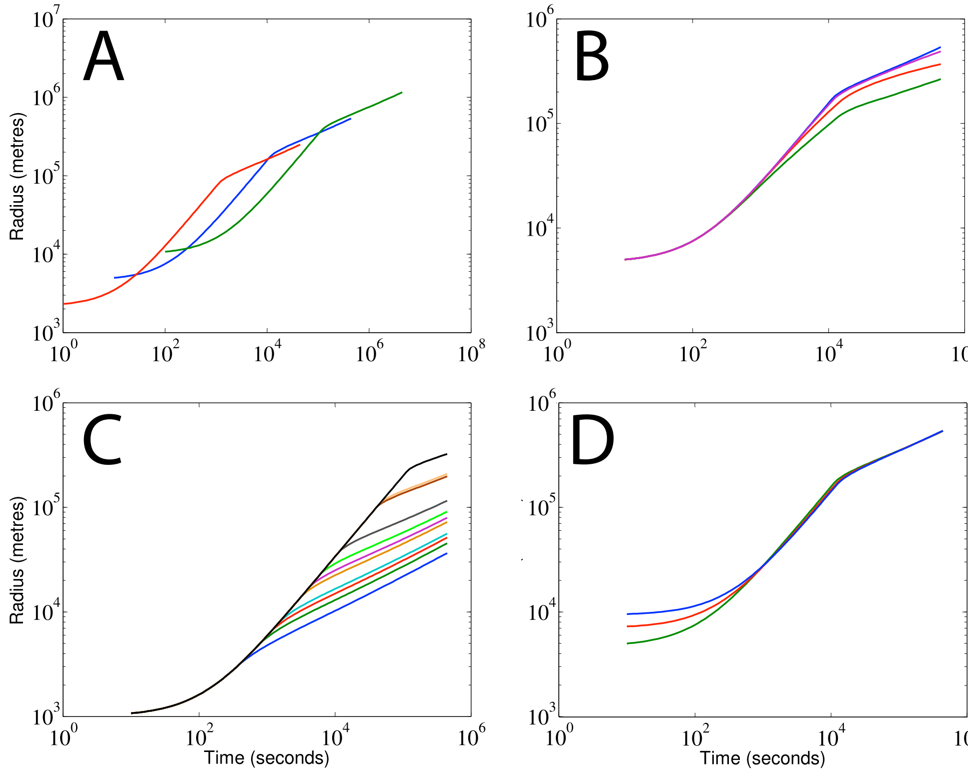

Figure 6: Effect of each of five parameters on results produced by the model. For each case, parameters not tested were fixed as follows: $N = 0.01\ s^{-1}$, $C_D = 0$, Duration $D = 2$ hours, $Q = 10^9\ m^3 s^{-1}$ and $r_0 = 1$ km. (a) Variation of buoyancy frequency, $N = 0.001\ s^{-1}$ (green line), $N = 0.01\ s^{-1}$ (blue line) and $N = 0.1\ s^{-1}$ (red line). (b) Variation of drag coefficient, $C_D = 0$ (blue line), $C_D = 0.001$ (purple line), $C_D = 0.01$ (red line) and $C_D = 0.1$ (green line). (c) Variation of duration of eruption, since $N = 0.01$ then $D = 3$ min (blue line), $D = 6$ min (green line), $D = 10$ min (red line), $D = 13$ min (light blue line), $D = 30$ min (orange line) $D = 40$ min (purple line), $D = 1$h (light green line), $D = 2$h (grey line), $D = 8$h (dark brown line), $D = 9$h (pink line) and $D = 24$h (black line). (d) Variation of volumetric flux/radian, $Q = 10^5\ m^3 s^{-1}$ (black line), $Q = 10^6\ m^3 s^{-1}$ (purple line), $Q = 10^7\ m^3 s^{-1}$ (green line), $Q = 10^8\ m^3 s^{-1}$ (red line)and $Q = 10^9\ m^3 s^{-1}$ (blue line). (e) Variation of the initial, nondimensional radius of intrusion, $r_0 = 1$ (green line), $r_0 = 1.5$ (red line) and $r_0 = 2$ (blue line). Slopes (power-law exponent) same as those shown in Fig. 5.

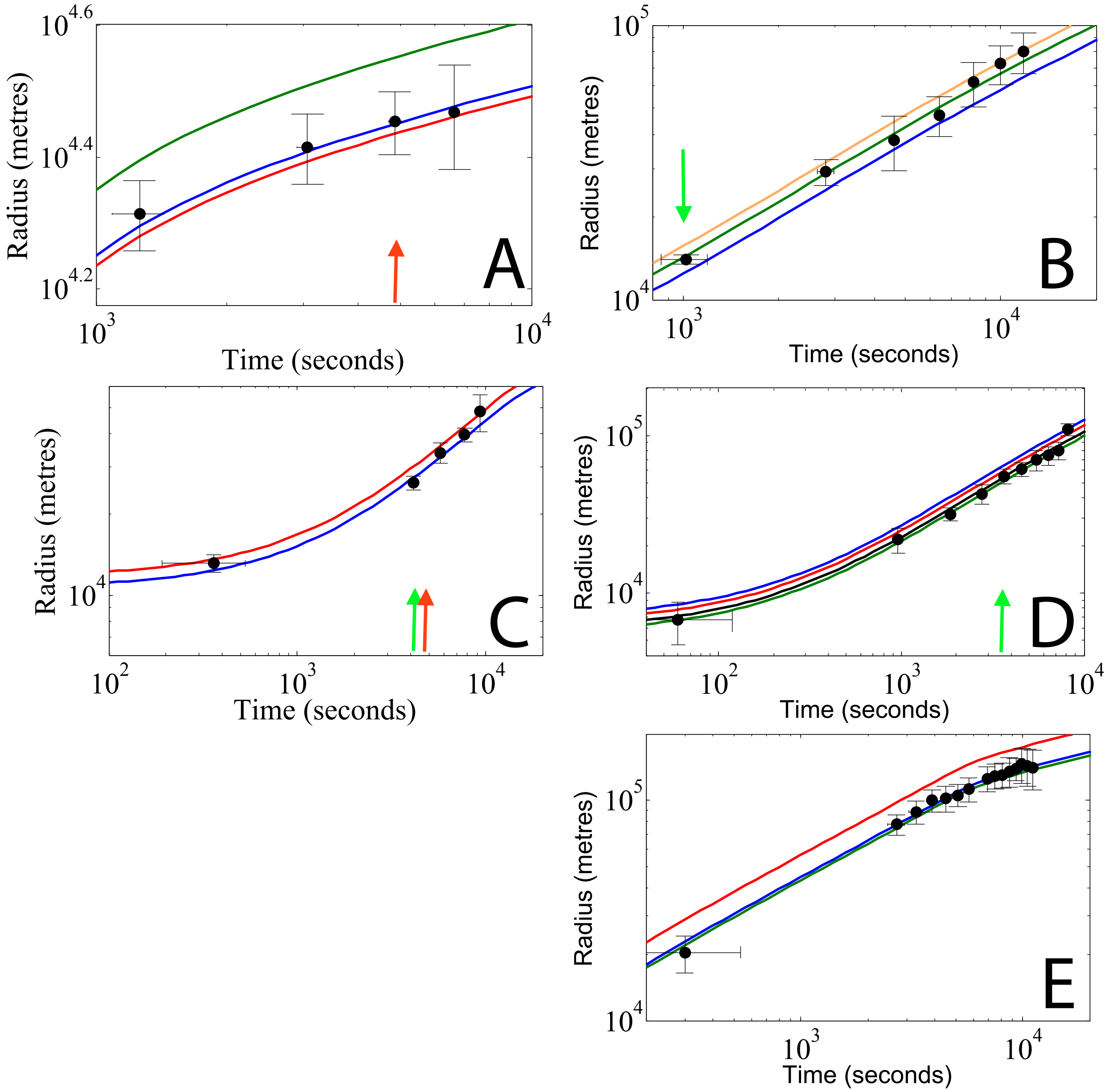

Figure 7: Comparison of cloud growth curves produced by model (full lines of different colors) and data measured from observed umbrella clouds (closed circles) with errorbars. (a) Shishaldin, 1999 ; (b) Okmok, 2008; (c) Sarychev Peak, 2009; (d) Grímsvötn, 2011 and (e) Kelut, 2014. Characteristics of each model run producing different colored curves given in Table 5. Green arrow, first satellite image in which smooth cloud appears (hypothesized start of gravity current flow); red arrow, end of eruption (D reached)

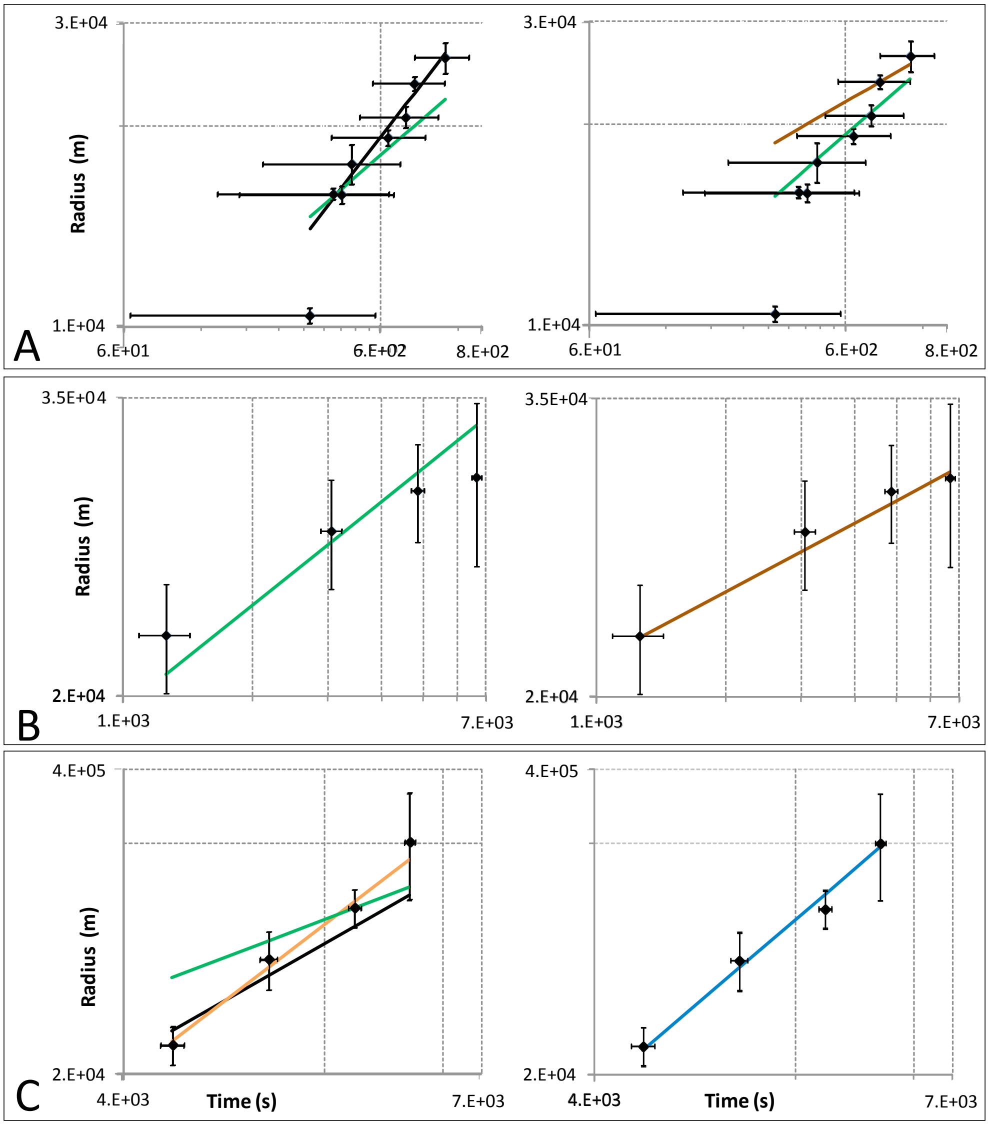

Figure 8: Evolution of the umbrella cloud radius with time (black diamonds) with associated error bars for short-lived eruptions using relationships from previous workers (left; Table 1) and from this work (right). (a) Redoubt, 1990; (b) Shishaldin, 1999; (c) Sarychev, 2009. First data point from Figure 7c removed as inconsistent with asymptotic behavior. Asymptotes are: $r_f \sim t^{2/9}$ (brown line), $r_f \sim t^{1/3}$ (green line), $r_f \sim t^{1/2}$ (black line), $r_f \sim t^{2/3}$ (orange line), $r_f \sim t^{3/4}$ (light blue line). Power-law curves from previous studies are on left side of figure, and power-law curves from present model on right side.

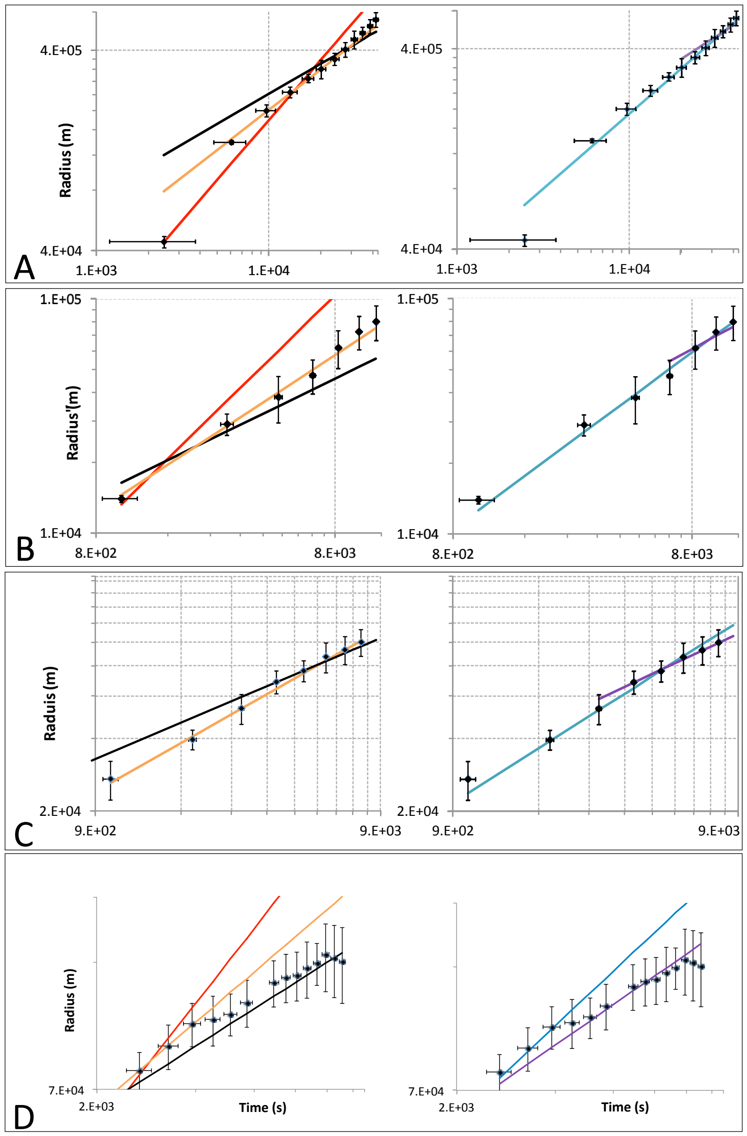

Figure 9: Evolution of umbrella cloud radius with time (black diamonds) with associated error bars for a long-lived eruption using relationships from previous workers (left; Table 2) and from this work (right). (a) Pinatubo, 1991; (b) Okmok, 2008; (c) Grímsvötn, 2011. First two data points from Figure 7d have been removed as potentially inconsistent with asymptotic behavior, (d) Kelut, 2014. First data point from Figure 7e removed for clarity. Asymptotes are: $r_f \sim t^{2/9}$ (brown line), curves $r_f \sim t^{1/2}$ (black line), $r_f \sim t^{5/9}$ (purple line), $r_f \sim t^{2/3}$ (orange line), $r_f \sim t^{3/4}$ (light blue line), $r_f \sim t$ (red line). Theoretical curves from previous studies are on left side of figure, and curves from present model on right side.

Appendix A. Drag-dominated intrusions of constant volume

After the cessation of an eruption, the volume of fluid in the plume remains approximately constant (increasingly only slowly due to entrainment), but buoyancy forces result in continued spreading. In the absence of drag, a buoyancy-inertial spreading regime becomes established Ungarish and Zemach (2007), with a radial growth rate of $t^{1/3}$. However, our numerical results (Fig. A.10) indicate that turbulent drag has often become significant by the point at which an eruption ceases, meaning that spreading of the plume will be drag-dominated. We calculate a similarity solution to the governing equations in this regime, which exhibits a radial growth rate of $r_f \sim t^{2/9}$. This derivation is analogous to that in (Johnson *et al.*, 2015) for the drag-dominated spread of an intrusion supplied by a constant flux.

After the eruption has ceased, there is no longer a volume flux per radian Q feeding the intrusion, so we nondimensionalize by scaling lengths to $V^{1/3}$, where V is the intrusion volume per radian, and times to N^{-1}, as before. At late times the governing equations (2) form a dominant balance in which buoyancy spreading forces are balanced by turbulent drag. In this regime, the governing equations become (in nondimensional form)

$$\frac{\partial h}{\partial t} + \frac{1}{r}\frac{\partial}{\partial r}(ruh) = 0 \qquad \text{and} \qquad \frac{h^2}{4}\frac{\partial h}{\partial r} = -C_D|u|u, \tag{A.1a,b}$$

respectively. We seek a similarity solution for these equations, and therefore first look for scalings. Integrating (A.1a) across the intrusion we find that $r_f^2 h \sim 1$, while from (A.1b) the balance between driving buoyancy forces and drag results in $h^3/r_f \sim C_D r_f^2/t^2$. These scalings suggest that $r_f \sim C_D^{-1/9} t^{2/9}$, and that a similarity solution may exist in which

$$h = \kappa C_D^{2/9} t^{-4/9} \mathcal{H}(\eta), \qquad u = \kappa C_D^{-1/9} t^{-7/9} \mathcal{U}(\eta), \qquad \text{and} \qquad r_f = \kappa C_D^{-1/9} t^{2/9}, \tag{A.2}$$

where $\eta = r/r_f(t)$ and κ is a dimensionless constant to be determined. On substitution of

(A.2) into the governing equations (A.1), we obtain

$$\frac{1}{\eta}\left(\eta\mathcal{U}\mathcal{H}\right)' - \frac{2\eta}{9}\mathcal{H}' - \frac{4}{9}\mathcal{H} = 0 \qquad \text{and} \qquad \frac{\mathcal{H}^2}{4}\mathcal{H}' = -\mathcal{U}|\mathcal{U}|. \tag{A.3a,b}$$

where the prime denotes differentiation with respect to η. These are subject to boundary conditions $\mathcal{U}(1) = 2/9$, representing the kinematic condition at the front, and $\mathcal{H}(1) = 0$, which is the frontal Froude number condition in the drag-dominated regime. Integrating (A.3a), and applying the kinematic condition, we find

$$\eta\left(\mathcal{U} - \frac{2\eta}{9}\right)\mathcal{H} = 0 \tag{A.4}$$

from which we deduce that $\mathcal{U} = 2\eta/9$. From (A.3b) we then find

$$\mathcal{H} = \left[\frac{16}{81}\left(1-\eta^3\right)\right]^{1/3}. \tag{A.5}$$

Profiles of the thickness and velocity of the plume, $\mathcal{H}$ and $\mathcal{U}$, are illustrated in Figure A.10. Equating the total volume of the intrusion per radian (expressed as a volume of revolution) with V, we obtain

$$\kappa^3 \int_0^1 \eta\mathcal{H}\,\mathrm{d}\eta = 1. \tag{A.6}$$

Evaluating (A.6) using (A.5), we find that $\kappa = 1.62\ldots$. Thus, in dimensional variables, the long time asymptotic radius of the intrusion is $r_f = 1.62(N^2V^3t^2/C_D)^{1/9}$.

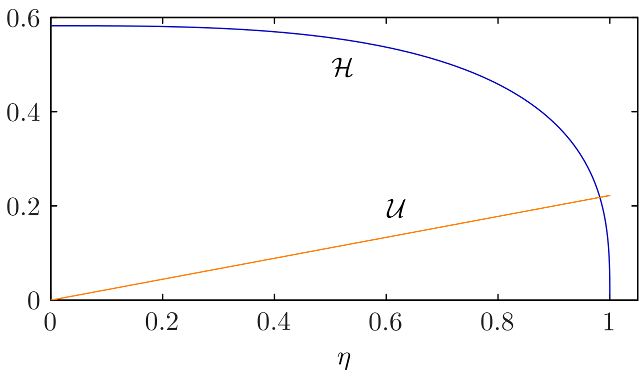

Figure A.10: Profiles of intrusion thickness $\mathcal{H}$ and radial velocity $\mathcal{U}$ for an intrusion of constant volume in a turbulent-drag dominated spreading regime.